



AFRL Additive Manufacturing Modeling Series: Challenge 4, In Situ Mechanical Test of an IN625 Sample with Concurrent High-Energy Diffraction Microscopy Characterization

David B. Menasche¹ · William D. Musinski² · Mark Obstalecki² · Megna N. Shah² · Sean P. Donegan² · Joel V. Bernier³ · Peter Kenesei⁴ · Jun-Sang Park⁴ · Paul A. Shade²

Received: 16 March 2021 / Accepted: 27 May 2021 / Published online: 9 June 2021
© The Minerals, Metals & Materials Society 2021

Abstract

We describe 3D characterization of an additively manufactured Inconel 625 nickel-base superalloy specimen conducted during a uniaxial tension test using a suite of nondestructive x-ray techniques. High-energy diffraction microscopy in both near- and far-field modalities are employed in situ to track evolution of the material orientation and stress–strain fields at six points during the mechanical test, and these data streams are registered with micro-computed tomography reconstructions which probe the material density. This data volume was matched to a multi-modal serial sectioning characterization of the specimen taken after loading, described in this article’s companion. Twenty-eight grains which were monitored throughout the experiment were selected to form the basis for AFRL AM Modeling Series Challenge 4, Microscale Structure-to-Properties.

Keywords HEDM · Computed tomography · Microstructure · Materials characterization · Synchrotron

Introduction

The past years have seen significant advancements in the suite of capabilities available for 3D non-destructive materials characterization, particularly at high-energy synchrotron x-ray sources, where simultaneous integration of diverse measurement modalities is the norm [1–5]. The combination of high-energy diffraction microscopy (HEDM) in both near-field (nf-HEDM) and far-field (ff-HEDM) modalities, together with micro-computed tomography (μ -CT) conducted concurrently, has proven effective at probing specimen microstructure at the mesoscale during in situ experiments. These in situ experiments explore material

performance under applied thermo-mechanical conditions of fundamental scientific and commercial interest. In particular, integration of HEDM methods with in situ mechanical testing allows the microstructure and mechanical state of a material to be tracked under prescribed loading conditions, which in turn provides critical information for the calibration and validation of materials performance models [6–9].

We harness these capabilities here to characterize a nickel-base superalloy specimen which is the subject of the Air Force Research Laboratory (AFRL) Additive Manufacturing (AM) Modeling Challenge Series [10, 11], Challenge 4. This challenge, “Microscale Structure-to-Properties,” provided participants with explicit 3D microstructural information and macroscopic mechanical test data, and asked them to model the micromechanical response of a specimen during a uniaxial tensile test. Specifically, participants were asked to predict the evolution of the grain-average elastic strain tensor for specific grains within the polycrystalline aggregate at specific loading states.

The material evaluated is additively manufactured Inconel 625 (IN625), a nickel-base superalloy of particular commercial and industrial interest [12]. Specimen diffraction and tomographic data were collected before, during, and after

✉ David B. Menasche
david.menasche@hamiltoniangroup.com

¹ Hamiltonian Group LLC, Washington DC 20007, USA

² Air Force Research Laboratory, Materials and Manufacturing Directorate, Wright-Patterson AFB, Ohio, OH 45433, USA

³ Lawrence Livermore National Laboratory, Engineering Directorate, Livermore, CA 94550, USA

⁴ Argonne National Laboratory, Advanced Photon Source, Lemont, IL 60439, USA

specimen tensile testing in order to measure the crystallographic orientation, material density, and grain-average elastic strain values within a volume of interest (VOI) at various times during uniaxial loading. Following these experiments, the same sample was serially sectioned, allowing for the final microstructure to be characterized with improved fidelity using optical and electron microscopy. These processes are described in a companion descriptor [13]. Ultimately, these data streams are combined and registered through post-processing into a spatially resolved volume which contains the full material crystallographic orientation, elastic strain, phase, and density fields [11, 14]. This volume was used as the starting microstructure for the micromechanical modeling challenge. Predicted strain tensor values were compared to the experimental strain tensor values described in the current manuscript to assess participant performance. Per the participation agreements set in place for the challenge, we are not publishing the results of individual participants, but rather allowing those participants to individually publish these results, either in the present special issue or elsewhere.

Continued use of this dataset for purposes of model development and validation is encouraged. The sample preparation, data collection, computational resources, and research labor requirements to produce such volumes are intensive, and this article is intended to be as much a guide and introduction to these data as it is a descriptor.

Experimental Methods

Sample Preparation

The AM material for this challenge was printed using commercially available IN625 gas-atomized powder and laser powder bed fusion with an EOS model M280 system. After deposition, the printed material was further processed with a stress relief heat treatment, followed by hot isostatic pressing and an additional annealing heat treatment. This additional processing optimized the as-built microstructure for measurement and tracking by the characterization modes described. The material processing parameters used for printing, hot isostatic pressing, and heat treatment are proprietary and intentionally undisclosed. A block of material, approximately $5 \times 5 \times 35 \text{ mm}^3$ in size, was shaped into a tensile sample geometry using wire electrical discharge machining. The approximate dimensions of the sample gauge volume are $0.5 \text{ mm} \times 0.5 \text{ mm} \times 1.0 \text{ mm}^3$ —a schematic of the prepared tensile test sample is depicted in Fig. 1b.

To assist with dataset post-processing and registration, as well as alignment throughout the in situ experiment, gold fiducial markers were affixed to the sample surface as described in Shade et al. [15]. These markers provide a contrasting x-ray absorption signature when compared to the

specimen material and are clearly identifiable using each imaging mode considered. A secondary electron SEM image of the sample surface with the three fiducial cubes affixed is shown in Fig. 1c, with the HEDM scanned VOI (discussed in Sect. Dataset reduction and analysis) highlighted by the shaded regions. Additional FIB-deposited platinum lines are visible in the figure, these were added after the in situ experiment and prior to the serial sectioning as described in Chapman et al. [13].

Characterization Modes

Characterization techniques utilized include nf-HEDM, ff-HEDM, digital image correlation, and phase- and absorption-contrast μ -CT. The x-ray techniques each used a monochromatic beam energy of 71.68 keV, corresponding to the Re k-shell edge. This beam energy was calibrated by placing Re foil into the beam-path and tuning the beam energy to maximize k-shell attenuation. These imaging modalities were conducted sequentially at each macroscopic load step using an identical experimental setup. For each modality, an appropriate detector was deployed and others were shielded or removed through beamline automation infrastructure. We discuss each imaging modality below.

HEDM

Both near- and far-field HEDM techniques utilize high-energy monochromatic x-rays to penetrate macroscopic sample volumes. A VOI is continuously illuminated by the x-ray beam while the specimen rotates about a fixed axis [16–18]. As crystallites satisfy the Bragg condition, they diffract and projections of grain shapes are collected on high-resolution area detectors located either a few mm from the sample rotation axis (as in nf-HEDM) or $\gtrsim 1000$ mm from the rotation axis (as in ff-HEDM). At close detector distances, the physical location of the diffracting volume is convolved with its orientation, which allows for computational recovery of the orientation and the volume's shape through forward modeling [19, 20]. As the distance between sample and detector grows larger (as in the far-field case), the shape of the diffracting volume is not recoverable, but identifying statistical deviations of a diffracted beam from its theoretical Debye–Scherrer position allows for computation of grain center-of-mass and grain-average elastic strain tensors [16, 21, 22]. With knowledge of the single crystal elastic moduli, stress tensors may be calculated from elastic strain tensors using Hooke's law.

nf-HEDM Refractive sawtooth lenses [23] were placed into the beam path to focus it into a ribbon (planar) beam approximately $0.002 \text{ mm high} \times 1.2 \text{ mm wide}$. The hori-

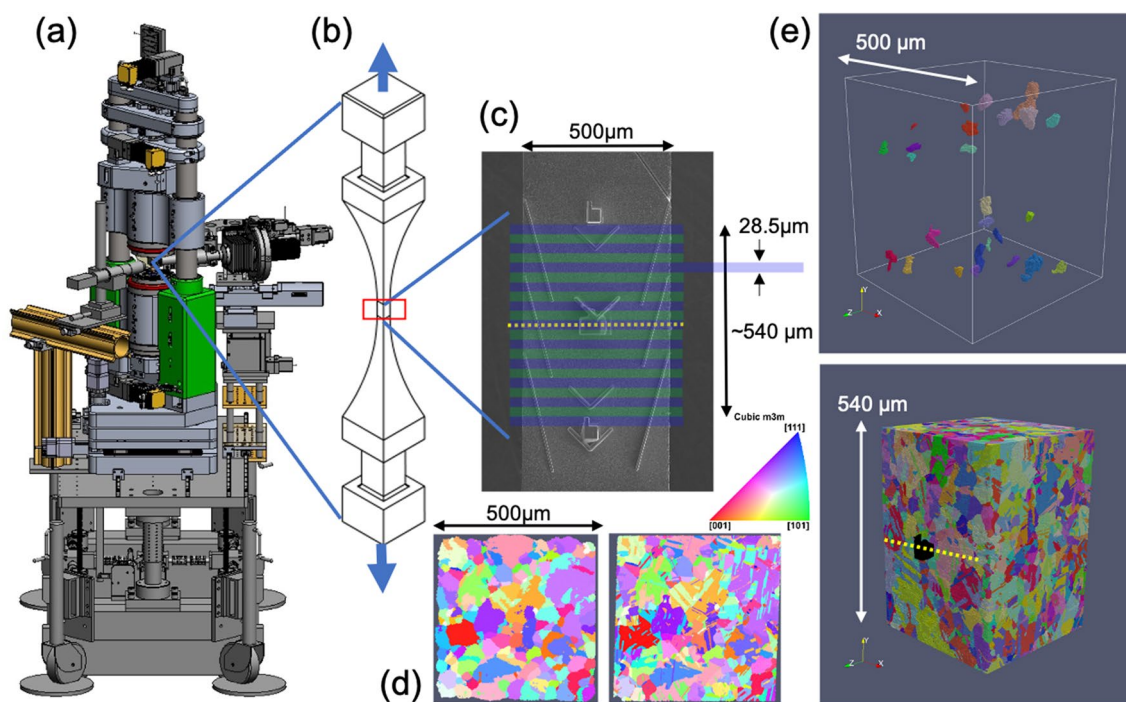


Fig. 1 Summary of the experiment conducted. In **a**, the RAMS3 rotation and axial motion system used to load and articulate the sample in the beampath. Schematically, the beam enters into the page at the origin of the blue rays and interacts with the sample volume held within the grips. A detector, depicted at right, records radiographic images emanating from the illuminated specimen. In **b**, a schematic of the IN625 specimen geometry, with the gauge volume of interest (VOI) highlighted by the red box, enlarges the measured volume of interest, depicting a scanning electron microscopy image of the sample surface to which the fiducial cubes and platinum tracks are

affixed. Shaded regions represent the scanned ff-HEDM subvolumes which were stitched together to form one data volume representing the microstructure in the VOI. The yellow-dashed line in **c** marks the center cross section of the VOI; snapshots of the microstructure at this location are pictured in **d** reconstructed using the nf-HEDM (left) and serially sectioned EBSD (right) measurements. The entire VOI is depicted in **e** at bottom and rendered from the EBSD data volume. The center fiducial gold cube is rendered black in the image foreground. At top, the 28 grains selected to form the basis for the Challenge 4 are highlighted within the volume

zonal dimension is defined by the width of adjustable slits which truncate the beam.

During near-field data collection, diffracted beams were collected on a high-resolution QImaging Retiga DC4000 CCD camera coupled to a LuAG:Ce optical scintillating screen. Objective lenses in the detector–scintillator system provide an effective pixel pitch of 1.48 μm on the 2048×2048 pixel CCD chip. The sample was rotated through a total angular range of 180° , and diffraction patterns were collected after every 0.25° rotation interval. Image exposure times were optimized prior to scanning to maximize the collected signal while avoiding detector saturation. In the near-field mode, diffraction patterns are collected at two or more sample-to-detector distances in order to resolve the origin of diffracted rays. These distances were found through optimization of the forward model to be approximately 5.8 and 7.8 mm. After measurement at each of these distances, the specimen is vertically translated through the beam-path and a new region may be scanned.

ff-HEDM The ff-HEDM diffraction patterns were collected on a four-panel array of GE Revolution 41RT detectors [24] located at a sample-to-detector distance of approximately 1900 mm. This configuration improves localization of the diffracted beams on the detector while increasing the measurement strain resolution compared to a one panel detector at roughly half the distance. The pixel pitch of the detectors is 200 μm .

During each scan, the specimen was rotated 360° about the loading axis, with diffraction patterns collected at 0.25° intervals. Scans were conducted using the $0.002 \text{ mm} \times 1.2 \text{ mm}$ planar beam described above in sect. nf-HEDM, but another mode was also utilized in which the lenses were removed and a $0.0285 \text{ mm} \times 1.2 \text{ mm}$ box beam was defined entirely with the adjustable slits. Similar to the nf-HEDM collection scheme, after each scan the sample was translated to illuminate a new region.

μ -CT

Micro-computed tomography (μ -CT) was performed to map the specimen’s material density field prior to load. Using the experimental geometry above in sect. HEDM, the sample was illuminated with a parallel x-ray beam while rotating 360° about its tensile axis. Exposures were collected on a CCD detector coupled to an optical scintillating screen. Analysis of the set of collected images provides a relative measure of the material density field in the illuminated VOI. Parallel x-rays passing through the sample are attenuated according to a path integral which varies by local material density. Rotating the sample and recording intensity variations for each ray generates a system of equations whose solution is proportional to the material density field.

The beam was prepared by removing the sawtooth lenses and defining the beam shape to be a comparatively tall box of dimensions 2 mm high \times 1.2 mm wide. This box was centered at the middle of the specimen gauge region, after which motorized translation stages facilitated the capture of white and dark field normalization images. Radiographs were captured every 0.25° over a 360° interval.

Distinct tomography detector configurations were utilized to collect images in both phase- and absorption-contrast modes. Absorption-contrast mode images were collected on the near-field detector at a sample-to-detector distance of 10 mm. Phase-contrast mode images were collected on a separate 2048 \times 2048 pixel imaging detector based on a Point Grey Grasshopper3 CMOS camera. A coupled objective lens and scintillator provide an effective pixel pitch of 1.172 μ m. This detector was placed 300 mm from the specimen. Automation of these detector stages facilitated the collection of these data without disturbance of the experimental setup.

Digital Image Correlation

The sample surface was imaged at each loading step using an Allied Vision Prosilica GX2750 camera, which provided 2750 \times 2200 pixel images at a pixel size of 4.54 μ m. A 6–12 \times objective zoom lens and a 1.5 \times lens attachment were also employed to capture the material region of interest within the field of view. These images were used for two-point digital image correlation to calculate the macroscopic strain values shown in Fig. 2.

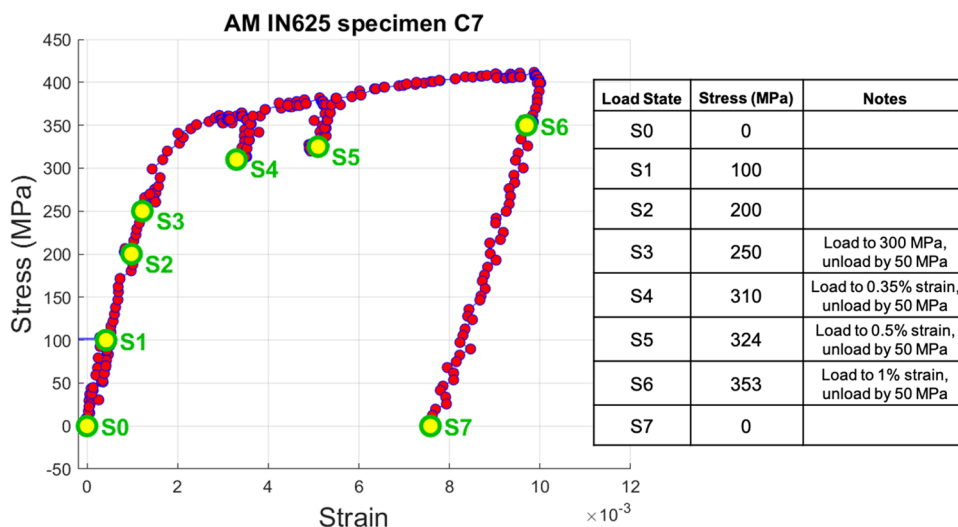
Experimental Overview

Sample tensile testing and x-ray characterization occurred during June 2018 at Argonne National Laboratory’s Advanced Photon Source, in experimental station E of Sector 1-ID. The experimental setup utilized the RAMS3 load frame, a third generation rotational and axial motion system that facilitates in situ material characterization. Depicted in a 3D computer-aided design (CAD) model in Fig. 1a, the RAMS3 precisely holds, translates, and rotates a test specimen within the x-ray beam during a concurrent mechanical test [25]. These motions do not affect the mechanical loading state of the sample.

Prior to mechanical loading, the specimen was mounted in customized grips which mate to the RAMS3 load frame. During sample mounting, negligible but finite forces are exerted on the microstructure. As the physical arrangement of the sample vis-a-vis the beam is the same for each of the x-ray characterization schemes described, once the sample was gripped, it was not disturbed from the load frame for the duration of the experiment.

To assist in specimen alignment and dataset registration, the gold fiducials on the sample surface were located in the x-ray beam by noting the differing absorption profile in the

Fig. 2 Specimen loading schedule, marked on the experimentally measured stress–strain curve. Characterizations of the specimen microstructure occurred at the marked points, S_i . At right, the corresponding values of macroscopic stress. For states S3 through S6, load was decreased from peak value by 50 MPa in order to prevent sample creep during x-ray characterization



beam intensity. A raw radiograph depicting the absorption profile of the sample is shown in Fig. 3a. Before each x-ray measurement, the center of the gauge region was identified by first recording the position of the direct line-focused beam profile on the Retiga detector. The focusing lenses are then removed to illuminate a wide sample volume, and the pixel position corresponding to the top surface of the middle gold fiducial was noted. The top surface position was then translated to the position identified with the center of the line-focused beam.

Prior to sample loading, μ -CT was performed in order to recover the initial material density field. Figure 3b illustrates a side-on view of this reconstructed μ -CT scan in which the highly x-ray absorbing gold is colored brightly against the more x-ray transparent IN625 specimen.

Data volumes were also collected in both near- and far-field modalities at zero applied load. A total of 19 subvolumes were scanned in the far-field mode, shown by the shaded regions in Fig. 1c. After each $\sim 30 \mu\text{m}$ -high volume was scanned, the sample was translated along the loading axis to illuminate a new volume. In total, this corresponded to a physical region of $\sim 540 \mu\text{m}$ along the specimen tensile axis. Fifteen planar scans at the vertical center of the specimen gauge region were also conducted in the far-field mode at a vertical spacing of $2 \mu\text{m}$. To assist with the registration of reconstructed far-field data to the serially sectioned reconstructions, 15 planar near-field scans were performed corresponding to those taken in the far-field mode.

Uniaxial tension was applied to the sample under displacement control, at a target strain rate of $1 \times 10^{-4} \text{ s}^{-1}$. Loading was paused at 6 points, to precisely reperform the series of box-beam ff-HEDM characterizations described above. These 6 points are labeled S_i on the experimental stress–strain curve pictured in Fig. 2 and are summarized by the schedule listed in the right inset. At measurement points occurring after material yield at around 350 MPa

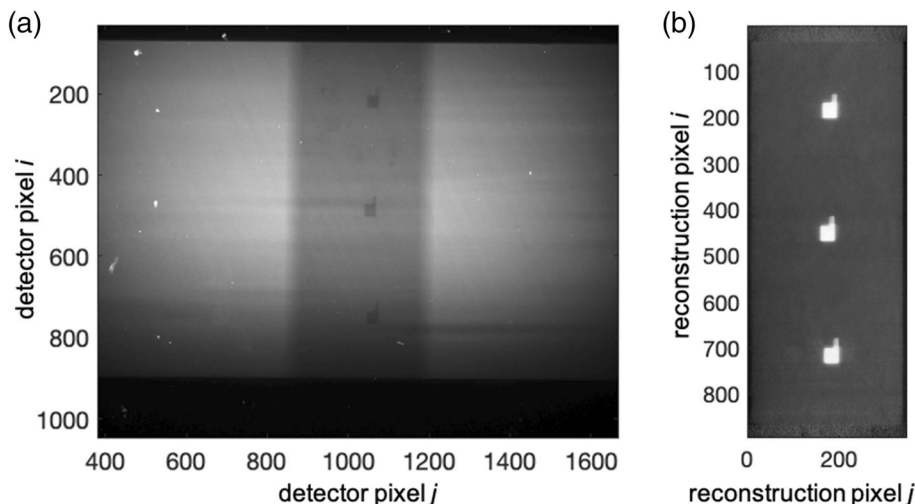
(S4–S6), applied stress was reduced by $\sim 50 \text{ MPa}$ to avoid creep during the measurement. As discussed, the gold fiducials attached to the specimen surface facilitated realignment of probed regions between load states. Digital image correlation data were collected and analyzed throughout each loading step in order to monitor total macroscopic strain.

During measurement S6, in addition to the box-beam scans, planar beam scans were conducted at the gauge center using near- and far-field HEDM. Fifteen planar scans, at a vertical spacing of $2 \mu\text{m}$, were taken in far-field mode, while the same region was probed using 7 near-field scans spaced at $4 \mu\text{m}$. At the conclusion of S6, the specimen was unloaded at a nominal strain rate of $1 \times 10^{-4} \text{ s}^{-1}$ until zero load was registered, at which point it was recharacterized, though these additional characterizations were not ultimately used to inform the Challenge. The S7 characterization consisted of a contiguous series of 25 planar scans collected in both near- and far-field modes. These planar measurements were spaced by $2 \mu\text{m}$ along the specimen loading axis.

Dataset Reduction and Analysis

Dataset reduction involves computationally reconstructing the relatively information-sparse diffraction and radiography images collected into material orientation, stress–strain, and density fields. The volume of data collected and the complexity of the diffraction problems considered dictate significant effort and infrastructure be dedicated to the tasks of reduction and coregistration. We will discuss first the tools and algorithms used to computationally reduce the data collected and will subsequently cover the methods used to coregister the recovered datastreams.

Fig. 3 At left, in **a**, a radiograph of the IN625 sample with the gold fiducial cubes affixed to the sample surface to facilitate alignment of the same VOI between scans. At right, **b** illustrates the surface of the specimen, as reconstructed from the μ -CT scan taken at S_0



HEDM Data Reduction

Far-field data were processed using the HEXRD software suite [26] on computer resources located at the beamline. This software tool uses the algorithm described in Bernier et al. [22] to computationally deduce grain orientation and center-of-mass information. Strain tensor values are then co-optimized with these quantities on a grain-by-grain basis to match the experimental data collected. Relative strains are resolved at precisions of approximately 1×10^{-4} , while orientation resolution is better than 0.05° . Crystallite centers-of-mass are determined to within about $50 \mu\text{m}$ for those that are equiaxed.

Near-field data reduction implementations utilize a compressed image format to increase computational tractability [27]. This preprocessing compression took place on beamline computing resources, and compressed images were transferred to AFRL Department of Defense Supercomputer Resource Center (DSRC) resources for further analysis. There, a computational forward model conducts a virtual experiment mirroring the one performed, and matches simulated diffracted beams to the compressed experimental diffraction images [19, 20]. The IceNine software package [28] was used for nf-HEDM reconstruction, compiled on the Mustang computing cluster. Each cross-sectional reconstruction utilized 6 node groups of 48 Intel Xenon Platinum computing cores for approximately three hours, a total expenditure of about 2×10^5 CPU hours.

As the origin of the simulated beam is known, spatial resolution is limited by detector characteristics and x-ray focusing capabilities. Grain boundaries are located under ideal measurement conditions to within $2 \mu\text{m}$ (just larger than one detector pixel), with orientation resolution better than 0.05° [29], though experimental time constraints precluded full expression of the technique for this case. Notably, some coherent twin structures were not captured, as is clear from comparison of the center fiducial layers in Fig. 1d.

μ -CT Data Reduction

Raw μ -CT data were analyzed on a beamline computing platform using the GridRec algorithm [30, 31]. Results from this method generate a relative measure of the material density. These relative values are saved as images which record intensity values at a particular cross section through the material volume. Like, the HEDM reconstructions, μ -CT reconstructions use the sample axis-of-rotation as a natural origin. Registration is straightforward and is achieved by scaling image pixels into a real-space coordinate representation. μ -CT has identified non-diffracting features like pores, voids, second phases, and inclusions within HEDM datasets, as in [32–34].

Reduced Data Processing Pathway

As a goal of the Challenge is to instantiate grain morphology into mesoscale modeling efforts that predict stress–strain response, the data streams described above required integration with the data volume discussed within this article's companion, which employed multi-modal serial sectioning. Particularly, our intent is to track the evolution of each grain's elastic strain tensor and to associate these measurements with the corresponding grains identified by examination of the serially sectioned data volume (SSDV). To achieve this, we cross reference grains identified from analysis of the ff-HEDM data with grains identified in the corresponding nf-HEDM data. The near-field data, with spatial resolution at the micron scale, is used as a bridge to identify corresponding grains in the SSDV. Use of this bridge helps especially to resolve non-bijective mappings between like orientations, as can occur when tracking similar orientations in a small region, as grains split into subgrains, or in highly twinned regions.

Prior to these steps, the data volumes representing each of the 19 contiguous ff-HEDM scans taken at each load state S_i required combination. Grains illuminated by the beam during multiple scans are computationally recovered multiple times, therefore an identification and merging process is implemented to identify a unique set of grains representing the specimen microstructure at S_i . Searching across these collections for grains of similar orientation and cross-referencing these by center-of-mass position or other criteria provides a robust method for grain tracking between reduced ff-HEDM data volumes representing each S_i state.

Merging of Each Far-Field Scan within a Single Load State

Each of the 19 box-beam scans taken at load states S_i characterizes the microstructure within the $0.0285 \text{ mm} \times 1.2 \text{ mm}$ box illuminated by the x-ray beam (see Fig. 1c). These were stitched together to form an approximately $540 \mu\text{m}$ tall volume by first applying a 2 degree scalar misorientation threshold between pairs of grain orientations in adjacent scans. Those grains which also had centers-of-mass within $50 \mu\text{m}$ when projected onto the beam plane were identified as connected elements. For grains that happened to span across multiple measurement layers, once the corresponding grain was identified within the near-field dataset, the elastic strain tensor values from each scan were averaged, with weights given by that grain's relative volume in each scan, as determined by analysis of the near-field maps.

Linking of the Experimental Volumes Across Load States

Data volumes were retained which represented each unique grain measured within the specimen microstructure at each

load state, S_i . Tracking the experimental evolution of a particular grain may be achieved by identifying a particular grain in S_i and then reidentifying it in S_{i+1} through a matching algorithm, as in Merging of each Far-Field Scan within a Single Load State.

Correlating Near-Field and Far-Field Microstructure Maps

The data volumes representing the reduced far-field data for each S_i were correlated to the microstructural maps recovered from the near-field data, using a matching algorithm similar to those described above. As the forward model is conducted without the assumption of grains per se, *i.e.*, each sample space voxel may be independently optimized for orientation, near-field orientation fields were first segmented according to a maximum two-degree grain-boundary definition criterion. Grain orientations were averaged according to [35], and a simplified list of grain orientation and center of mass corresponding to the 1000 largest grains (sphere-equivalent radius $\gtrsim 19 \mu\text{m}$) were retained to check against the merged S_0 far-field data volume.

Orientation and elastic strain data contained in the S_0 volume were transformed into the coordinate reference frame of the near-field experiment for dataset registration procedures, and corresponding pairs of orientations from each dataset were matched using a two-degree misorientation threshold criterion. These grain pairs were retained, thus creating a traversable linkage between the near-field orientation field reconstructions and the volumes S_i containing reduced far-field grain orientations and elastic strain tensor values. Ultimately, grain orientations and strain tensors were provided in the far-field experimental frame for the Challenge.

Correlating Near-Field Microstructure Maps with the SSDV

The SSDV was furnished by the collaborator-coauthors of this article's companion, [13]. It contains full 3D microstructure orientation field information from the serially sectioned measurement at a voxel size of $2 \mu\text{m}$. Reconstruction of the SSDV required analysis of multiple microscopy signals, including electron backscatter diffraction mapping, backscatter electron imaging, and optical imaging. The SSDV may be visualized as a 3D image with each voxel containing material characterization values of interest. Matching this data to the near-field orientation maps involved mapping each voxel in the image to a point in physical space and comparing the lattice orientation within that voxel to the orientation given by the near-field map at that physical location. In the absence of systematic distortions in either of the datasets, a single affine transformation would be sufficient to scale, rotate, and translate the SSDV into alignment with the near-field maps [28].

Serial sectioning of the sample took place essentially parallel to the beam plane implying rotation about the specimen loading direction (beam plane normal) would align physical coordinates between the two datasets. This transformation was determined by comparing the location of the gold fiducials in each. Physical coordinates and orientations in the SSDV were rotated according to this transformation, but as in [30], an additional axis mirroring was applied to the spatial coordinates to bring the two into coincidence. This additional axis mirroring stems from alignment conventions between spatial and orientation reference frames within the EBSD indexing software.

Integrated point-to-point misorientation was computed between the SSDV and the collection of near-field maps in order to guide the optimization of alignment between the two datasets. Points at which misorientation is below a five-degree threshold were chosen to represent pairs of aligned and corresponding grains found in both datasets. Identifying these unique pairs over the 3D data volume linked corresponding grains in the near-field maps and SSDV, thereby completing a “lookup table” of grains tracked through all characterization modes. A total of 3170 grain pairs were identified. Two-dimensional orientation field maps from the nf-HEDM and SSDV which represent the sample microstructure at the center fiducial are illustrated in Fig. 1d. Grains are colored with respect to the stereographic triangle pictured for the $\langle 001 \rangle$ inverse pole. Note, the absence of certain coherent twin features in the nf-HEDM reconstruction relative to the SSDV microstructure in part motivates the need for the higher spatial resolution serial sectioning characterization.

Choice of Grains of Interest for Challenge 4

Several criteria were applied as filters in order to select grains of particular interest to model for the challenge. Grains were considered which were identified in the SSDV and were tracked unambiguously across all S_i . A grain is considered “unambiguously tracked” from state S_i if there is one and only one grain in S_{i+1} which satisfies the conditions in sects Linking of the Experimental Volumes Across Load States. Grains not completely contained within the SSDV were disallowed; grains which were relatively equiaxed and not highly twinned or with particularly re-entrant morphologies were preferred. Following application of these filters, 28 grains were chosen on which to base the challenge. These 28 challenge grains along with the entire SSDV are pictured in Fig. 1e top and bottom, respectively.

The grain-averaged elastic strain evolution for each of the challenge grains is tracked across all load states. This allows for the comparison of the distribution of each component of strain, shown in Fig. 4. On each horizontal axis, load states S_i are plotted. At each of these states, a violin plot illustrates

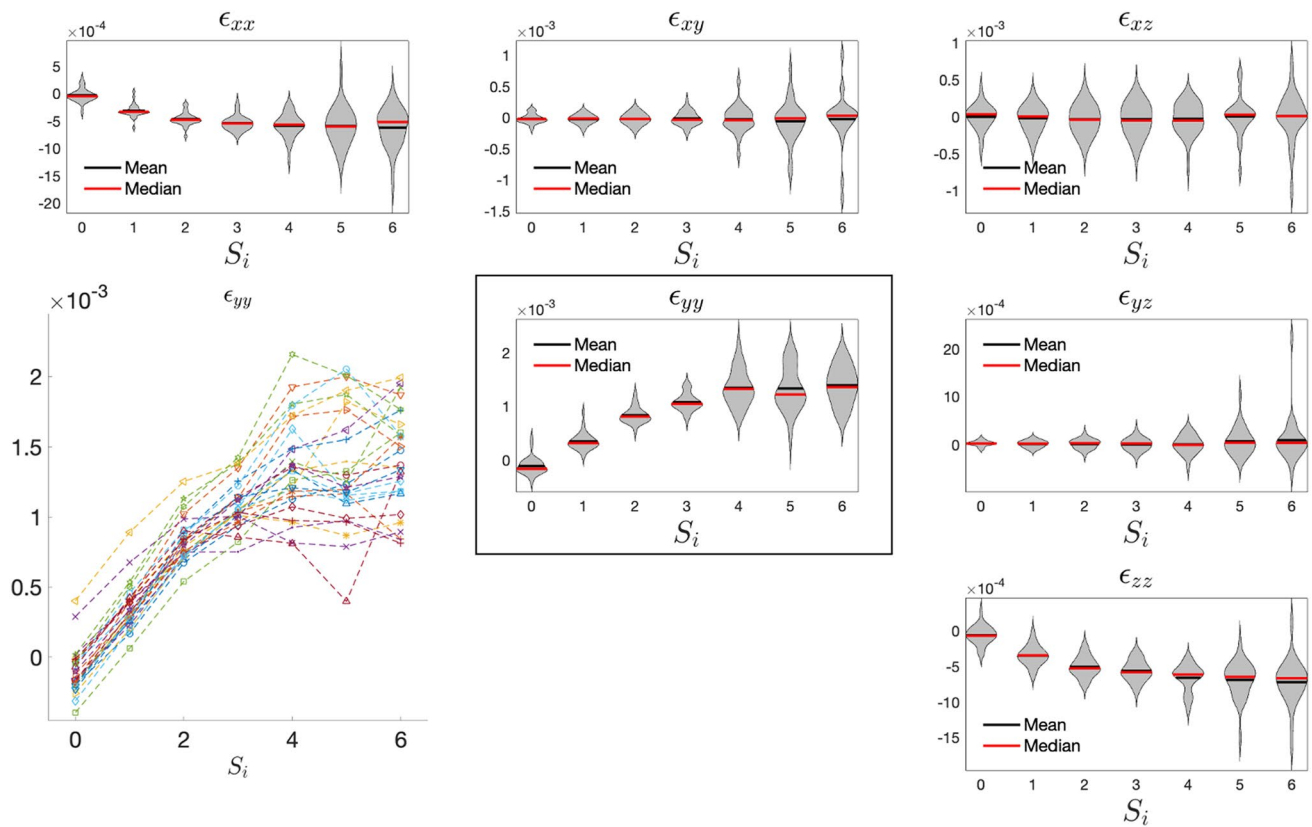


Fig. 4 Violin plots illustrate the evolving distribution of each strain component within the set of challenge grains. Each violin represents a smoothed histogram of the distribution of strain component values at each load state S_i . The mean and median are marked by black and red lines, respectively. In the inset, we track the ϵ_{yy} principal axis strain

a smoothed histogram of the distribution of each strain component for the 28 challenge grains. These distributions illustrate a general broadening at increasing load, indicating a heterogeneous response between grains examined. The strain component ϵ_{yy} is parallel to the direction of applied uniaxial tension. Inset at left, the individual trajectories shown for each challenge grain illustrate that individual grain load states are not monotonically increasing, i.e., that the local stress–strain response within the material does not always match that of the bulk.

Conclusion

A series of 3D in situ non-destructive material characterizations were performed on an additively manufactured, IN625 specimen during uniaxial tensile loading. The material microstructure, including orientation and stress–strain fields, were characterized six times during loading, and the evolution of the micromechanical elastic strain states of constituent grains were associated with a data volume of

for challenge grains across S_i and look to observe plasticity through stress relaxation within individual grains or through the behavior of groups. Note, the orders of magnitude on the plots vary by strain component

orientation information obtained by serial sectioning. The resulting data volume was utilized to instantiate and validate image-based materials performance models as a part of AFRL AM Modeling Challenge Series, Challenge 4.

Acknowledgements DBM, WDM, MO, MNS, SPD, JVB, and PAS acknowledge support from the United States Air Force Research Laboratory (AFRL). DBM is thankful for the high-performance computer time and resources provided by the AFRL DoD Supercomputing Resource Center (DSRC) that supported HEDM reconstructions performed in this work. The authors acknowledge technical discussions and logistical support from Marie Cox (AFRL, program manager for AFRL AM Modeling Series). Edwin Schwalbach (AFRL) and Michael Groeber (Ohio State University, previously employed at AFRL) are acknowledged for technical discussions and providing the AM material. Michael Uchic (AFRL) is acknowledged for technical discussions and serial sectioning coordination. Sirina Safriet (UDRI) and Basil Blank (Pulseray) are acknowledged for help with specimen preparation. Jon Almer, Ali Mashayekhi, and Kurt Goetze (Argonne National Lab) are acknowledged for support of the beamline experiment. This research used resources of the Advanced Photon Source, a U.S. Department of Energy (DOE) Office of Science User Facility operated for the DOE Office of Science by Argonne National Laboratory under Contract No. DE-AC02-06CH11357.

Declarations

Conflict of interest The authors declare that they have no conflict of interest.

References

- Ludwig W, King A, Reischig P, Herbig M, Lauridsen EM, Schmidt S, Proudhon H, Forest S, Cloetens P, Rolland du Roscoat S, Buffière JY, Marrow TJ, Poulsen HF (2009) New opportunities for 3D materials science of polycrystalline materials at the micrometre lengthscale by combined use of X-ray diffraction and X-ray imaging. *Mater Sci Eng, A* 524(1–2):69–76. <https://doi.org/10.1016/j.msea.2009.04.009>
- Lienert U, Li SF, Hefferan CM, Lind J, Suter RM, Bernier JV, Barton NR, Brandes MC, Mills MJ, Miller MP, Jakobsen B, Pantleon W (2011) High-energy diffraction microscopy at the advanced photon source. *JOM* 63(7):70–77. <https://doi.org/10.1007/s11837-011-0116-0>
- Poulsen H (2012) An introduction to three-dimensional X-ray diffraction microscopy. *J Appl Crystallogr* 45:1084–1097. <https://doi.org/10.1107/S0021889812039143>
- Schuren JC, Shade PA, Bernier JV, Li SF, Blank B, Lind J, Kenesei P, Lienert U, Suter RM, Turner TJ, Dimiduk DM, Almer J (2015) New opportunities for quantitative tracking of polycrystal responses in three dimensions. *Curr Opin Solid State Mater Sci* 19(4):235–244. <https://doi.org/10.1107/S0021889812039143>
- Bernier JV, Suter RM, Rollett AD, Almer JD (2020) High-energy X-ray diffraction microscopy in materials science". *Annu Rev Mater Res* 50(1):395–436. <https://doi.org/10.1146/annurev-matsci-070616-124125>
- Pokharel R, Lind J, Li SF, Kenesei P, Lebensohn RA, Suter RM, Rollett AD (2015) In-situ observation of bulk 3D grain evolution during plastic deformation in polycrystalline Cu. *Int J Plast* 67:217–234
- Shade PA, Musinski WD, Obstalecki M, Pagan DC, Beaudoin AJ, Bernier JV, Turner TJ (2019) Exploring new links between crystal plasticity models and high-energy X-ray diffraction microscopy. *Curr Opin Solid State Mater Sci* 23(5):100793. <https://doi.org/10.1016/j.cossms.2019.07.002>
- Miller MP, Pagan DC, Beaudoin AJ, Nygren KE, Shadle DJ (2020) Understanding micromechanical material behavior using synchrotron X-rays and in situ loading. *Metall Mater Trans A* 51:4360–4376. <https://doi.org/10.1007/s11661-020-05888-w>
- Proudhon H, Pelerin M, King A, Ludwig W (2020) In situ 4D mechanical testing of structural materials: the data challenge. *Curr Opin Solid State Mater Sci* 24(4):100834. <https://doi.org/10.1016/j.cossms.2020.100834>
- Groeber M (2018) A preview of the U.S. Air Force research laboratory additive manufacturing modeling challenge series. *JOM* 70(4):441–444. <https://doi.org/10.1007/s11837-018-2806-3>
- Cox, M.E., Schwalbach, E.J., Blaiszik, B.J. et al. AFRL Additive Manufacturing Modeling Challenge Series: Overview. *Integr Mater Manuf Innov* (2021). <https://doi.org/10.1007/s40192-021-00215-6>
- Pollock TM, Tin S (2006) Nickel-based superalloys for advanced turbine engines: chemistry, microstructure and properties. *J Propul Power* 22:361–374
- Chapman MG, Shah MN, Donegan SP, Scott JM, Shade PA, Menasche DB, Uchic MD (2021) AFRL Additive manufacturing modeling series: challenge 4, 3D reconstruction of an IN625 high-energy diffraction microscopy sample using multi-modal serial sectioning. *Integr Mater Manuf Innov* 17:1–20. <https://doi.org/10.1007/s40192-021-00212-9>
- Shade PA, Musinski WD, Shah MN, Uchic MD, Donegan SP, Chapman MG, Park JS, Bernier JV, Kenesei P, Menasche DB, Obstalecki M, Schwalbach EJ, Miller JD, Groeber MA, Cox ME (2019) AFRL AM modeling challenge series challenge data package. Mater Data Facility. <https://doi.org/10.18126/K5R2-32IU>
- Shade PA, Menasche DB, Bernier JV, Kenesei P, Park J-S, Suter RM, Schuren JC, Turner TJ (2016) Fiducial marker application method for position alignment of in situ multimodal X-ray experiments and reconstructions. *J Appl Crystallogr* 49:700–704. <https://doi.org/10.1107/S1600576716001989>
- Poulsen HF, Nielsen SF, Lauridsen EM, Schmidt S, Suter RM, Lienert U, Margulies L, Lorentzen T, Juul Jensen D (2001) Threedimensional maps of grain boundaries and the stress state of individual grains in polycrystals and powders. *J. Appl. Cryst.* 34:751–756. <https://doi.org/10.1107/S0021889801014273>
- Poulsen HF (2004) Three-dimensional X-ray diffraction microscopy: mapping polycrystals and their dynamics. Springer, Berlin
- Ludwig W, King A, Herbig M, Reischig P, Marrow J, About L, Lauridsen EM, Paulson H, Buffire JY (2010) Characterization of polycrystalline materials using synchrotron X-ray imaging and diffraction techniques. *JOM* 62(12):22–28
- Suter RM, Hennessy D, Xiao C, Lienert U (2006) Forward modeling method for microstructure reconstruction using X-ray diffraction microscopy: single-crystal verification. *Rev Sci Instrum* 10(1063/1):2400017
- Li SF, Suter RM (2013) Adaptive reconstruction method for three-dimensional orientation imaging. *J Appl Crystallogr* 46(2):512–524. <https://doi.org/10.1107/S0021889813005268>
- Oddershede J, Schmidt S, Poulsen HF, Sørensen HO, Wright J, Reimers W (2010) Determining grain resolved stresses in polycrystalline materials using three-dimensional X-ray diffraction. *J Appl Phys* 43:539–549. <https://doi.org/10.1107/S0021889810012963>
- Bernier JV, Barton NR, Lienert U, Miller MP (2011) Far-field high-energy diffraction microscopy: a tool for intergranular orientation and strain analysis. *J Strain Anal Eng Design* 46(7):527–547. <https://doi.org/10.1177/2F0309324711405761>
- Shastri SD, Kenesei P, Mashayekhi A, Shade PA (2020) Focusing with saw-tooth refractive lenses at a high-energy X-ray beamline. *J Synchrotron Radiat* 27(3):590–598. <https://doi.org/10.1107/S1600577520003665>
- Lee JH, Almer J, Aydiner C, Bernier JV, Chapman K, Chupas P, Haeflner D, Kump K, Lee PL, Lienert U, Miceli A, Vera G (2007) Characterization and application of a GE amorphous silicon flat panel detector in a synchrotron light source. *Nucl Instrum Methods Phys Res, Sect A* 582(1):182–184. <https://doi.org/10.1016/j.nima.2007.08.103>
- Shade PA, Blank B, Schuren JC, Turner TJ, Kenesei P, Goetze K, Suter RM, Bernier JV, Li SF, Lind J, Lienert U, Almer J (2015) A rotational and axial motion system load frame insert for in situ high energy X-ray studies. *Rev Sci Instrum* 86:093902. <https://doi.org/10.1063/1.4927855>
- <https://github.com/joelvbernier/hexrd>
- Lind J, Rollett AD, Pokharel R, Hefferan CM, Li SF, Lienert U, Suter RM (2017) Image processing in experiments on, and simulations of plastic deformation of polycrystals. In: Proceedings of IEEE international conference on image processing. IEEE
- Li SF. IceNine. <https://github.com/FrankieLi/IceNine>
- Menasche DB, Shade PA, Suter RM (2020) Accuracy and precision of near-field high-energy diffraction microscopy forward-model-based microstructure reconstructions. *J Appl Crystallogr* 53(1):107–116
- Wang Y, De Carlo F, Foster I, Inslay J, Kesselman C, Lane P, von Laszewski G, Mancini DC, McNulty I, Su M, Tieman B (1999)

- Quasi-real-time X-ray microtomography system at the advanced photon source. *SPIE Proceedings* 3772:318
31. De Carlo F, Albee PB, Chu YS, Mancini DC, Tieman B, Wang SY (2002) High-throughput real-time X-ray microtomography at the advanced photon source. In: *SPIE proceedings*, volume 4503
 32. Menasche DB, Shade PA, Lind J, Li SF, Bernier JV, Kenesei P, Schuren JC, Suter RM (2016) Correlation of thermally induced pores with microstructural features using high energy X-rays. *Metall Mater Trans A* 47:5580–5588
 33. Menasche DB, Lind J, Li SF, Kenesei P, Bingert JF, Lienert U, Suter RM (2016) Shock induced damage in copper: a before and after, three-dimensional study. *J Appl Phy* 119: <https://doi.org/10.1063/1.4947270>
 34. Naragani D, Sangid MD, Shade PA, Schuren JC, Sharma H, Park J-S, Kenesei P, Bernier JV, Todd TJ, Parr I (2017) Investigation of fatigue crack initiation from a non-metallic inclusion via high energy X-ray diffraction microscopy. *Acta Mater* 137:71–84. <https://doi.org/10.1016/j.actamat.2017.07.027>
 35. Cho JH, Rollett AD, Oh KH (2005) Determination of a mean orientation in electron backscatter diffraction measurements. *Metall Mater Trans A* 36:3427–3438. <https://doi.org/10.1007/s11661-005-0016-4>

Publisher's Note Springer Nature remains neutral with regard to jurisdictional claims in published maps and institutional affiliations.